Chalcogenide Letters Vol. 19, No. 12, December 2022, p. 965 - 977

Synthesis and electrocatalytic performance for hydrogen evolution reaction of $ReSe_2$ nanosheets

X. Y. Zhang[a], J. Liu[a], Y. D. He[a], Z. Liu[a], A. X. Wei[a,b,*]

[a]*School of Integrated Circuits, Guangdong University of Technology, Guangzhou 510006, Guangdong, China*

[b]*School of Information and Intelligent Engineering, Guangzhou Xinhua University, Dongguan 523133, Guangdong, China*

Two-dimensional $ReSe_2$ as catalyst for hydrogen evolution reaction (HER) has attracted attention due to its unique 1T′ structure and anisotropic physical properties in base planes. In this work, $ReSe_2$ nanosheets were directly prepared on a carbon cloth (CC) substrate by hydrothermal synthesis technology. The reaction solution was prepared using ammonium perrhenium (NH_4ReO_4), sodium borohydride ($NaBH_4$), selenium (Se) powder and deionized water. The effects of reactant concentrations and reaction time on the catalytic properties of the $ReSe_2$ /CC for HER were researched. When the concentration of NH_4ReO_4, Se and $NaBH_4$ is 0.05 M, 0.065 M and 0.200 M, $ReSe_2$/CC shows the optimal HER catalytic properties with overpotential of 197 mV at current density of 10mAcm^{-2}, Tafel slope of 142 mVdec^{-1} and ECSA of 325cm^2. The formation mechanism and working mechanism in the HER process of $ReSe_2$/CC are discussed.

(Received September 27, 2022; Accepted December 22, 2022)

Keywords: Rhenium diselenide, Hydrothermal synthesis, Electrocatalys, Hydrogen evolution reaction

1. Introduction

The widespread use of fossil fuels in modern industry has led to serious problems such as resource depletion, carbon dioxide emissions and environmental pollution. To solve these problems, hydrogen (H_2) has been considered an ideal alternative to fossil fuels because of its renewable, free-pollution and sustainable [1, 2]. The hydrogen evolution reaction (HER) from electrocatalytic water splitting is an efficient and clean method to generate H_2 [3]. However, the HER from electrocatalytic water splitting needs high-efficient, low-cost and stable electrocatalys to decrease the overpotential and increase the reaction rate. Platinum (Pt), iridium (Ir) and Ruthenium (Ru) are good HER electrocatalysts, among which Platinum is the best HER catalyst owing to its Gibbs free energy (ΔG_{H*}) of hydrogen adsorption being close to 0 [4, 5]. However, the high price and scarcity limit their practicality. Therefore, developing high-performance HER electrocatalysts is very essential to promote the HER process.

Two-dimensional (2D) transition metal chalcogenides (TMDs) with an X-M-X layered structure (molecular formula MX_2; M represent transition metal; X represent S, Se and Te) have been considered as a promising electrocatalyst for HER due to their low cost, high stability and good HER catalytic activity [6, 7]. 2D Rhenium-based TMDs （ReX_2, X= S or Se ） are a unique member among the TMD family. Unlike most TMDs with the 2H phase structure, 2D ReS_2 and

* Corresponding author: 985931304@qq.com

https://doi.org/10.15251/CL.2022.1912.965

$ReSe_2$ have a pristine distorted triclinic symmetric 1T′ phase crystal structure and unique anisotropic physical properties in-plane, such as anisotropic charge carrier mobility [8-9]. In 1T′ phase crystal structure, Re atoms form rhomboid Re_4 clusters and Such Re–Re σ bond induces the formation of diamond shaped Re_4 clusters. The strong Re−Re σ bond of Re-based TMDs is beneficial to improve electrocatalytic HER properties due to its extra electron [11, 12]. Moreover, distortions of Re atoms away from their ideal octahedral positions cause rather weak interlayer coupling. Therefore, ReX_2 is layer number-independent direct band gap semiconductor [13]. The unique structure and unusual properties of 2D ReX_2 have shown good application prospects as catalysis for HER process [14-16]. However, there are still inherent shortcomings such as a relatively low number of active sites and poor electrical conductivity. The HER catalytic activity of 2D ReX_2 can be improved by increasing their number of active sites and enhancing their electrical conductivity. The number of active sites of 2D ReX_2 can be increased by creating Re or S/Se vacancies, defects [17-19] and doping transition metal atoms [20, 21]. For example, Sofer et al. [19] exfoliated 2D ReS_2 and $ReSe_2$ flakes using sodium naphthalenide as an exfoliation agent, and then S/Se vacancies were introduced by electrochemical pretreatments in sulfuric acid. Their experimental results indicated that the electrochemical treatment can be employed to produce chalcogen vacancies with HER catalytic active and improve the electrocatalytic performance of 2D ReX_2, which was further proved by DFT theoretical calculation. Kwak et al. [21] reported that the 10% Mo-doped $ReSe_2$ shows highest HER catalytic activity with overpotential of 77 mV at current density of 10 $mAcm^{-2}$ and a Tafel slope of 42 $mVdec^{-1}$ in 0.5 M H_2SO_4 electrolyte. DFT calculation demonstrated that Mo atoms near Se vacancies are HER active sites due to favoring the Mo−H bond formation. In addition, improving electrical conductivity of 2D ReX_2 can facilitate the charge transfer capacity and enhance the HER performance of catalyst. For example, Yoo et al. [22] designed and prepared few-layered $ReSe_2$ nanoflakes vertically anchored on a reduced graphene oxide (rGO) nanosheet by hydrothermal method. The $ReSe_2$@rGO catalyst shows excellence HER performance with a overpotential of 145.3 mV at 10 $mAcm^{-2}$ and a Tafel slope of 40.7 $mVdec^{-1}$ due to rGO improving electrical conductivity, facilitating electron transport and suppressing self-aggregation of $ReSe_2$ nanoflakes.

Herein, $ReSe_2$ nanaosheets were directly prepared on CC substrate using one-step hydrothermal synthesis. The reaction solution used in hydrothermal reaction was prepared by dissolving ammonium perrhenium (NH_4ReO_4), sodium borohydride ($NaBH_4$), selenium (Se) powder into deionized water. The effects of reactant concentrations and reaction time on the catalytic properties of the $ReSe_2$ /CC for HER were investigated.

2. Experimental

2.1. Preparation and characterization of the $ReSe_2$ nanosheets

Carbon cloth is purchased from Taiwan Carbon Energy Technology Co. Ltd. The weight density, thickness and sheet resistance of carbon cloth are 120 gm^{-2}, 0.33mm and 5 $m\Omega cm^2$, respectively. $ReSe_2$ nanosheets were directly grown on CC substrate using one step hydrothermal method. Briefly, 1.0 mmol of NH_4ReO_4, 1.3 mmol Se powder and 4 mmol of $NaBH_4$ were dissolved into 60 ml of deionized water and stirred until a transparent reaction solution was formed. The reaction solution was poured into a 100 ml PTFE liner, and the cleaned carbon cloth

(10 mm×10mm) was vertically placed into the PTFE-lined stainless-steel autoclave reactor. The hydrothermal reaction continues 8 h at 200 ℃. The sample was removed and rinsed several times with deionized water and alcohol, and then was dried at 60 °C in ambient air. Two sets of samples were prepared at different concentration of precursor solutions and different growth time, and the preparation process conditions are provided in Table 1.

The morphology of $ReSe_2$ nanosheets was observed using scanning electron microscopy. The crystallographic structure of the $ReSe_2$ nanosheets was analyzed using Raman spectroscopy and transmission electron microscopy. The element distribution map, chemical state and atom ratio of Se to Re elements in the $ReSe_2$/CC were analyzed using energy dispersive spectroscopy (EDS) and X-ray photoelectron spectroscopy (XPS). The instrument model used is described in the supporting information.

Table 1. Preparation process parameters of $ReSe_2$ nanosheets.

Sample No	NH_4ReO_4 mmol	Se mmol	$NaBH_4$ mmol	Water ml	Temperature ℃	Reaction time h
C1	1	1.3	4	60	200	8
C2	2	2.6	8	60	200	8
C3	2.5	3.25	10	60	200	8
C4	3	3.9	12	60	200	8
D1	2	2.6	8	60	200	6
D2	2	2.6	8	60	200	8
D3	2	2.6	8	60	200	10
D4	2	2.6	8	60	200	12

2.2. Electrochemical measurements of $ReSe_2$/CC

An electrochemical work station (CHI660E, Shanghai Chenhua) was used to test the electrocatalytic HER performance of $ReSe_2$/CC in a 1 M KOH of electrolyte solution using a classical three-electrode system. $ReSe_2$/CC (10 mm ×10 mm), Hg/HgO and graphite (20 mm x 20 mm) were employed as the working electrode, reference electrode and counter electrode, respectively. To activate and stabilize the catalyst, cyclic voltammetry (CV) test are carried out several times until the curves overlap. Linear scanning voltammetry (LSV) was measured in the range from -1.4 V to -0.9 V (vs Hg / HgO) and 95% IR correction was performed. Cyclic voltammetry (CV) was tested in the non-Faraday range from -0.9 V to -0.8 V (vs Hg / HgO) at different scan rates from 10 mVs^{-1} to 50 mVs^{-1}. Electrochemical impedance spectroscopy (EIS) is performed at frequency range from 10^{-2} Hz to 10^{5} Hz. The details electrocatalytic measurements are described in Supporting Information (SI).

3. Results and discussions

3.1. Morphology and structure analysis of the $ReSe_2$ nanosheets

Fig.1 shows SEM images of $ReSe_2$ nanosheets prepared using different precursor concentrations (all reactant concentrations are increased to double, two and a half or triple of the

initial concentration). $ReSe_2$ grown directly on CC substrates by hydrothermal method is composed of numerous nanosheets which gather into flower-like microspheres. The diameter of the microspheres is in the range of 50-100nm. However, the distribution of these flower-like microspheres on the CC substrate is not uniform enough, and some aggregation phenomenon occurs. When the concentration of NH_4ReO_4, Se and $NaBH_4$ is 0.017 M, 0.022 M and 0.067 M, respectively1 (sample C1), $ReSe_2$ nanosheets have fully covered the CC substrate, When all reactant concentrations increase to double of the initial concentration (sample C2), the aggregation of $ReSe_2$ nanosheets appears.

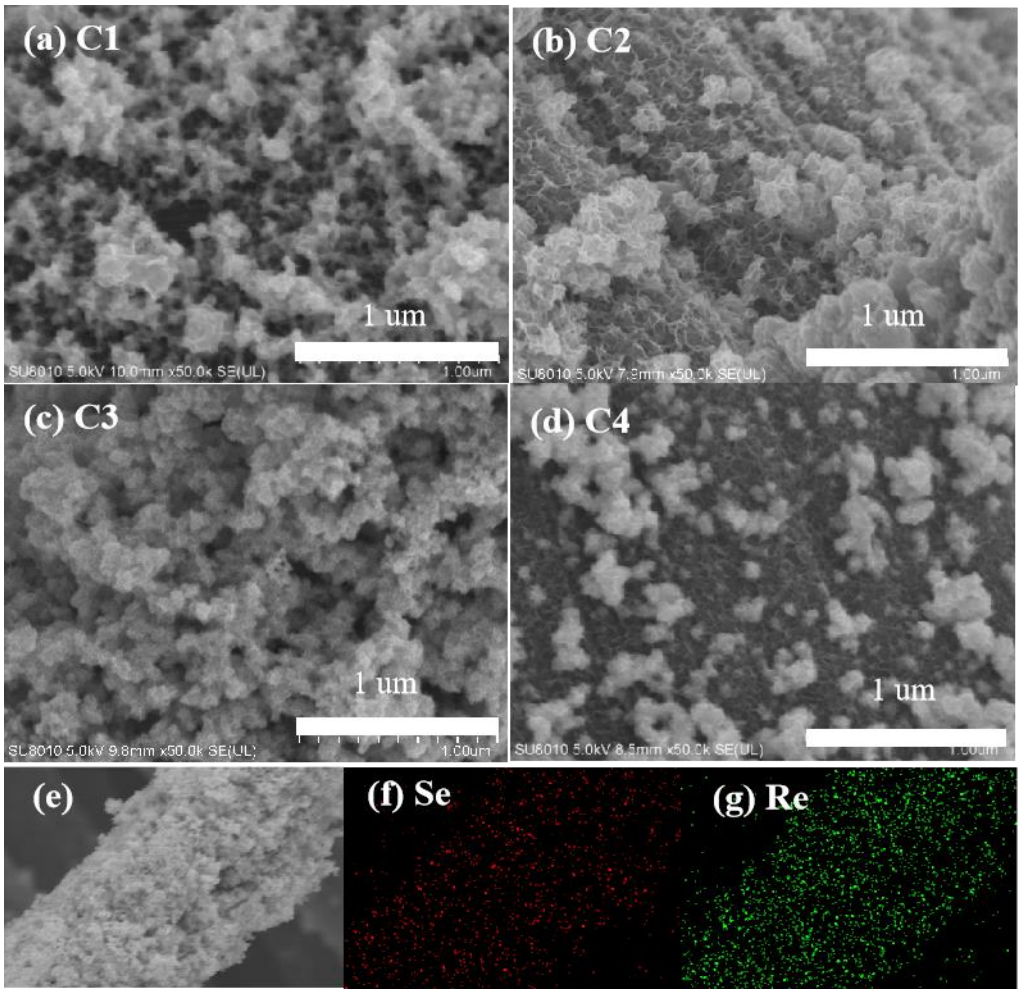

Fig. 1. (a-d) SEM images of samples prepared at different reactant concentration; (e) Low magnification SEM image; (f, g) Se and Re elemental mapping images.

When all reactant concentrations are further increased to two and a half time or triple (samples C3 and C4) of the initial concentration, the thickness of $ReSe_2$ nanosheets significantly increased, and the more serious aggregation occurs. The SEM images of samples prepared at growth time from 6 h to 12 h are presented in Fig.S1 (SI). With the prolonging the growth time, the diameter of the flower-like microspheres increased slightly, however agglomeration phenomenon also occurs. Fig.S2 (SI) provides the SEM image of blank CC and low magnification SEM image of all samples. The concentrations of NH_4ReO_4, $NaBH_4$ and Se in reaction solution

obviously affect distribution density of $ReSe_2$ nanosheets on a carbon cloth. The thickness of $ReSe_2$ increases as increasing concentration of reactants. However, the aggregation phenomenon also increases. Compared with the concentration of the reactants, the growth time has a slight effect on the thickness and aggregation of $ReSe_2$.The elemental distributions of $ReSe_2$ were observed by energy dispersion spectroscopy (EDS). Fig. 1e-g provides SEM image and EDS elemental mapping of Re and Se for the $ReSe_2$ nanosheets. It can be clearly observed that the Re and Se elements are uniform distribution over the entire $ReSe_2$ nanosheets.

The crystal structure of the $ReSe_2$ nanosheets was further characterized using high-resolution transmission electron microscopy (HRTEM) and selected area electron diffraction (SAED). Fig.2 gives the TEM image, HRTEM images and SEAD of $ReSe_2$ nanosheets, respectively. Fig.2a shows that $ReSe_2$ is composed of many very thin nanosheets which are highly consistent with result observed from SEM images in Fig.1. The interlayer diffraction fringe and the diffraction fringe of the base plane can be observed in Fig2 b. The measured fringe spacing is approximately 0.62nm which is corresponding to interlayer spacing of 2D layered $ReSe_2$ with a 1T' phase structure. The layer number of $ReSe_2$ nanosheets is approximately 3-5 layers. Fig.2c provides the magnified HRTEM image of basal plane. The interplanar spacing of 0.25 nm is corresponding to the $(\bar{2}02)$ crystal plane of the 1T' phase $ReSe_2$.

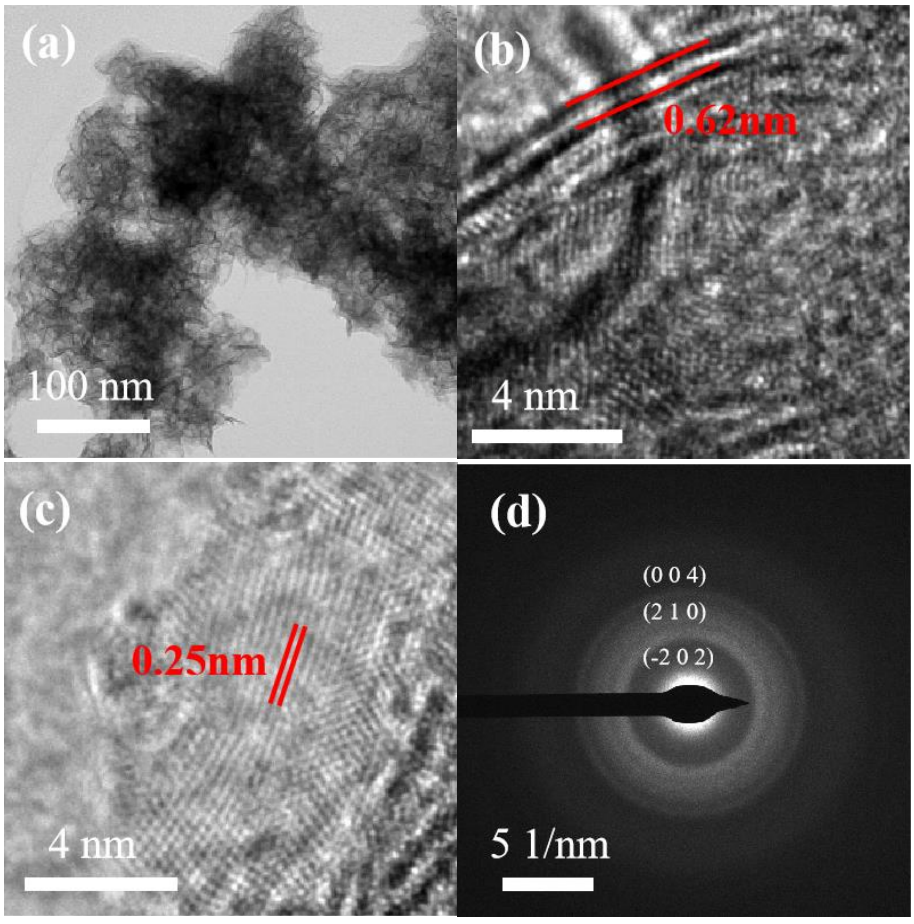

Fig. 2. (a) TEM; (b, c) HRTEM; (d) SEAD of $ReSe_2$ nanosheets.

Fig.2d provides SAED pattern of $ReSe_2$ nanosheets. The SAED pattern of 2D $ReSe_2$ nanaosheets shows three dim diffraction rings which are corresponding to (202), (210) and (004) crystal planes of 1T' phase $ReSe_2$, respectively, which indicates that the prepared $ReSe_2$ nanosheets is polycrystalline with grain size of several nanometers. Therefore, the base planes of $ReSe_2$ nanosheets have many grain boundaries, resulting in intrinsic defects such as Re or Se vacancies.

The structure of the $ReSe_2$ nanosheets was characterized by Raman spectroscopy. Raman spectrum of $ReSe_2$ nanosheets is shown in Fig.3a Raman peaks located at 115 and 122 cm^{-1} are ascribed to in-plane E_g-like vibrational modes, and Raman peaks at 158，172, 179, 217, 230, 239，248，261, 283 and 292cm^{-1} are assigned to out-of-plane A_g-like vibrational modes[23].These characteristic peaks are very similar to those of $ReSe_2$ flakes mechanically exfoliated [24] and synthesized by CVD [25, 26]. The chemical state and elemental distribution of the $ReSe_2$ nanosheets were analyzed using XPS and EDS. Fig.3b displays the XPS full spectrum of $ReSe_2$ /CC. Except for C, N, O elements from the substrate and adsorbed air, the sample contains only Re and Se elements. The atomic ratio of Se to Re is 2.9 which indicate the existence of Re vacancies. Fig.3c and Fig.3d show the high-resolution XPS spectra of Re 4f and Se 3d, respectively. Re $4f_{5/2}$ and Re $4f_{7/2}$ are located at 44.52 eV and 42.13 eV with peak difference of 2.39 eV, which is consistent with binding energy of an oxidation state of Re^{+4}. A broad peak at 55.54 eV is ascribed to Se 3d which could be fit by two bands using 20% Lorentzian-Gaussian function (open circles are XPS raw data, black lines are fitted data), the blue and red bands correspond to Se $3d_{5/2}$ and Se $3d_{3/2}$ states, respectively.

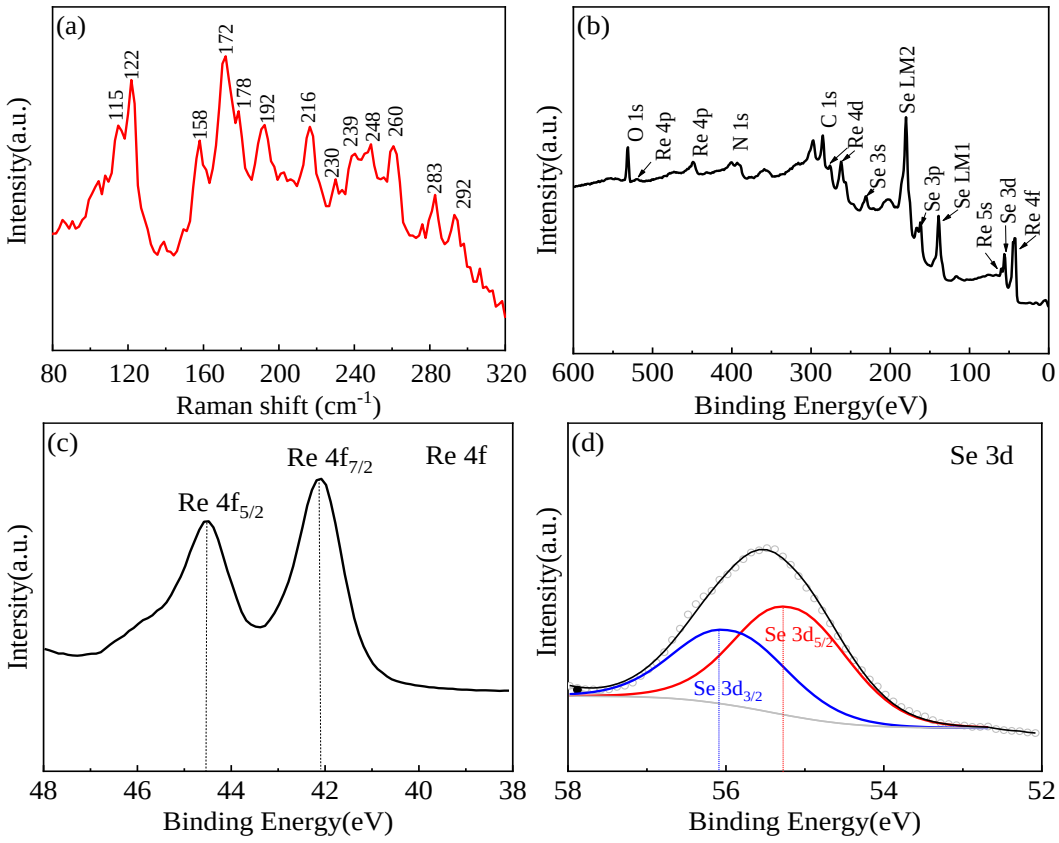

Fig. 3. (a) Raman spectra of $ReSe_2$ nanosheets; (b) XPS survey spectrum; (c) Re4f high-resolution spectrum; (d) Se3d high-resolution spectrum.

3.2. Electrocatalytic HER properties of $ReSe_2$ nanosheets

Electrocatalytic HER properties of $ReSe_2$ nanosheets prepared at different the precursor concentration were investigated using electrochemical workstation with three-electrode system in 1 M KOH electrolyte. Fig.4a displays the LSV polarization curves of samples; their overpotential at 10 $mAcm^{-2}$ is 264, 246, 238 and 197 mV for sample C1, C2, C3 and C4, respectively. Sample C4 exhibits a lowest overpotentiall of 197 mV at 10 $mAcm^{-2}$. Fig. 4b shows Tafel plots (η- log j) of samples which are draw according to LSV curves in Fig.4a. Tafel slope is estimated by fitting the linear part in Fig.4b. The Tafel slope values of samples are given in Fig.4b and Table S2. The Tafel slope is an important parameter used to describe the reaction rate of HER process. Small Tafel slope reflects fast electron transport capability and strong HER kinetics. Based on experimental data, it is found that sample C4 has the smallest overpotential and Tafel slope among the four samples, indicating that the HER activity of sample C4 is better than the other samples. As observed from SEM images in Fig.1 and Fig.S2 (SI), the thickness of $ReSe_2$ grown on CC substrate increases with increasing the concentrations of NH_4ReO_4, $NaBH_4$ and Se in the precursor solution, resulting in HER catalytic activity of sample gradually increases.

Cyclic voltammetry (CV) is another analytical method to characterize the electrocatalytic performance of catalyst. The electric double layer capacitance (C_{dl}) and electrochemical surface area (ECSA) of the catalyst can be obtained by CV measurement. The CV curves of samples measured at different scanning rates are provided in Fig.S3 (SI). Difference in current density at 0.07 V vs. RHE are plotted against scan rate in Fig.4c.

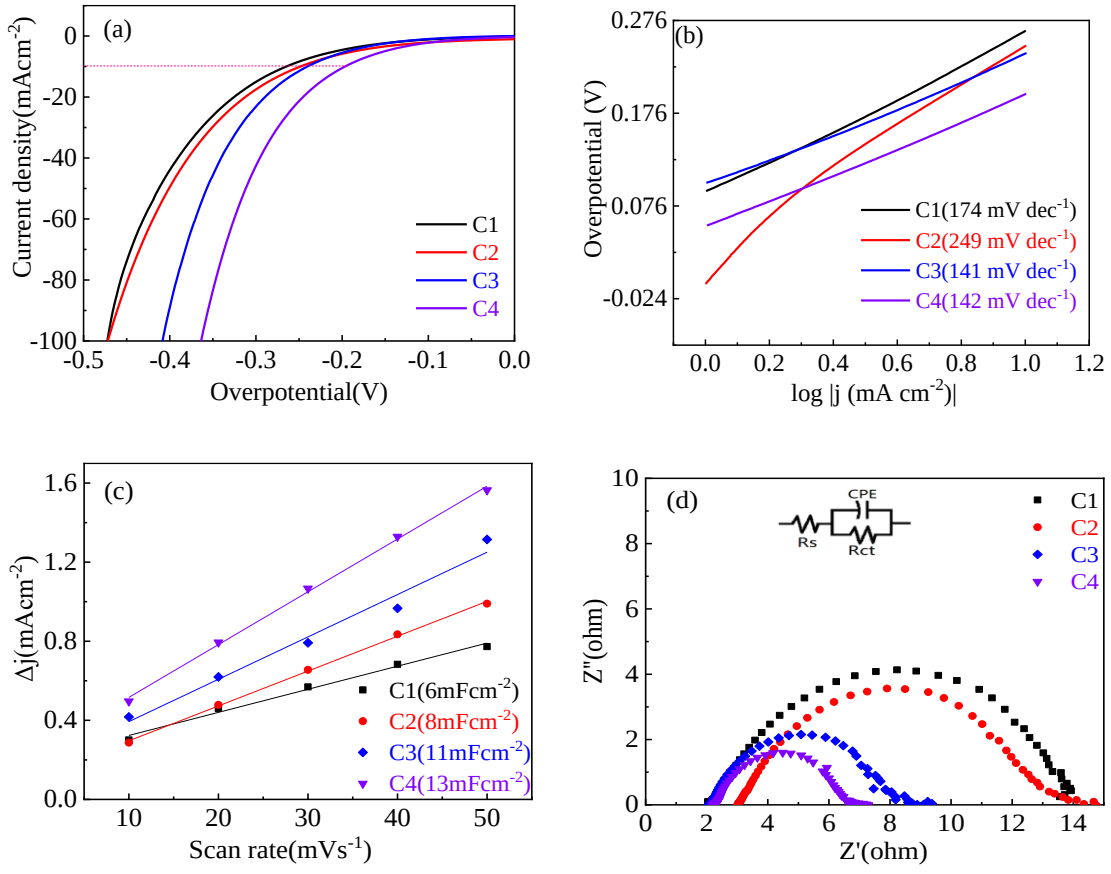

Fig. 4. Electrocatalytic HER performance of samples C1, C2, C3 and C4: (a) LSV curve; (b) Tafel slope curve; (c) Dependence of current density with scan rate; (d) Nyquist plot.

The double-layer capacitance C_{dl} can be obtained by fitting the slope of a linear part. The C_{dl} value calculated from Fig. 4c are 6, 8, 11 and 13 $mFcm^{-2}$ for samples C1, C2, C3 and C4, respectively. ECSA is linearly proportional to C_{dl}. The relationship between ECSA and C_{dl} can be expressed by the following formula [27, 28]

$$\mathrm{ECSA} = \frac{\mathrm{C_{dl}}}{\mathrm{C_S}} = \frac{\mathrm{C_{dl}}}{40\mu\mathrm{Fcm^{-2}per cm_{ESCA^{-2}}}} \quad (1)$$

where C_s is the specific capacitance. C_s is generally in the range of 20-60μFcm^{-2} [27], C_s is taken to be 40 μFcm^{-2} in this work.. According to equation (1), the ESCA values are 150, 200, 275 and 325 cm^2 for samples C1, C2, C3 and C4, respectively. The larger ECSA is corresponding to the more surface active sites of catalyst. The sample C4 exhibits the largest ECSA. Therefore, the results obtained by CV analysis are consistent with those obtained by LSV analysis. The charge transport capacity of the samples was further analyzed using electrochemical impedance spectroscopy (EIS). Nyquist plots of samples are provided in Fig.4d. The measured data are fitted to an equivalent circuit shown in the inset in Fig.4d using Z-view software. In equivalent circuit model, R_s represent the resistance of electrolyte; R_{ct} represent the charge transfer resistance at the interface between the $ReSe_2$/CC catalyst and KOH electrolyte, and the C_{PE} represents the capacitance. The R_s, R_{ct} and C_{PE} obtained by the fitting-calculated are given in Table S1 (SI). The average resistance of electrolyte is 2.75Ω. R_{ct} values are 10.09, 8.07, 5.77 and 4.13Ω for samples C1, C2, C3 and C4, respectively. In general, good contact between catalyst and substrate lead to the small R_{ct}. The smaller the R_{ct} at the catalyst-electrolyte interface, the faster the charge transfer kinetics and the better the catalytic activity of the catalyst. Therefore, the sample C4 exhibits the best electrocatalytic HER property which can be ascribed to the fastest charge transfer kinetics and the most active sites. C_{PE} values are 3.05, 8.74, 11.12 and 15.76 mF/cm^2, which are close to C_{dl} values obtained by CV testing. J. Li and coworkers [29] prepared vertically aligned $ReSe_2$ nanosheets directly on carbon cloth（CC） and black glass carbon (BGC) by using chemical vapor deposition method. For $ReSe_2$/CC catalyst，the overpotential at 10 $mAcm^{-2}$, Tafel slope, C_{dl} and R_{ct} are 265 mV, 69 $mVdec^{-1}$, 9.6 $mFcm^{-2}$ and 142.4 Ω for the HER process in a 0.5 M H_2SO_4 electrolyte, respectively. While for $ReSe_2$/BGC catalyst, they are 303 mV, 120 $mVdec^{-1}$, 0.55 $mFcm^{-2}$ and 435.1 Ω，respectively. The electrocatalytic HER performance of our $ReSe_2$/CC sample is superior to that of their sample, which is attributed to the fact that the contact resistance between the hydrothermally prepared $ReSe_2$ nanosheet and CC substrate is much smaller than that of the CVD-prepared vertically aligned $ReSe_2$ nanosheets and CC substrate. Yoo et al. [22] designed and synthesized $ReSe_2$ nanoflakes vertically anchored on a reduced graphene oxide (rGO) by hydrothermal method. The $ReSe_2$/rGO shows overpotential of 202 mV at a current density of 10 $mAcm^{-2}$, a Tafel slope of 61.6 $mVdec^{-1}$, double-layer capacitance C_{dl} of 3.5 $mFcm^{-2}$ and charge transfer resistance of 55.2 Ω for the HER process in a 0.5 M H_2SO_4 electrolyte.

To further evaluate the effect of growth time on the electrocatalytic HER properties of the $ReSe_2$/CC, LSV, CV and EIS measurements were carried out for samples D1, D2, D3 and D4, and the results are displayed in Fig.S4. The overpotential, Tafel slope, double-layer capacitance C_{dl}, electrochemical surface area ECSA and charge transfer resistance R_{ct} are listed in Table S1 (SI) for all samples. The experimental results indicate that sample D3 displays the highest electrocatalytic HER activity, so we can infer that the electrocatalytic performance of $ReSe_2$ nanosheets is

continuously improved with the prolonged growth time in the range from 6 h to 10 h. Nevertheless, with the growth time further up to 12 h, the electrocatalytic HER performance of $ReSe_2$ nanosheets will attenuate due to the agglomeration of $ReSe_2$ nanosheets hindering the transfer of electrons.

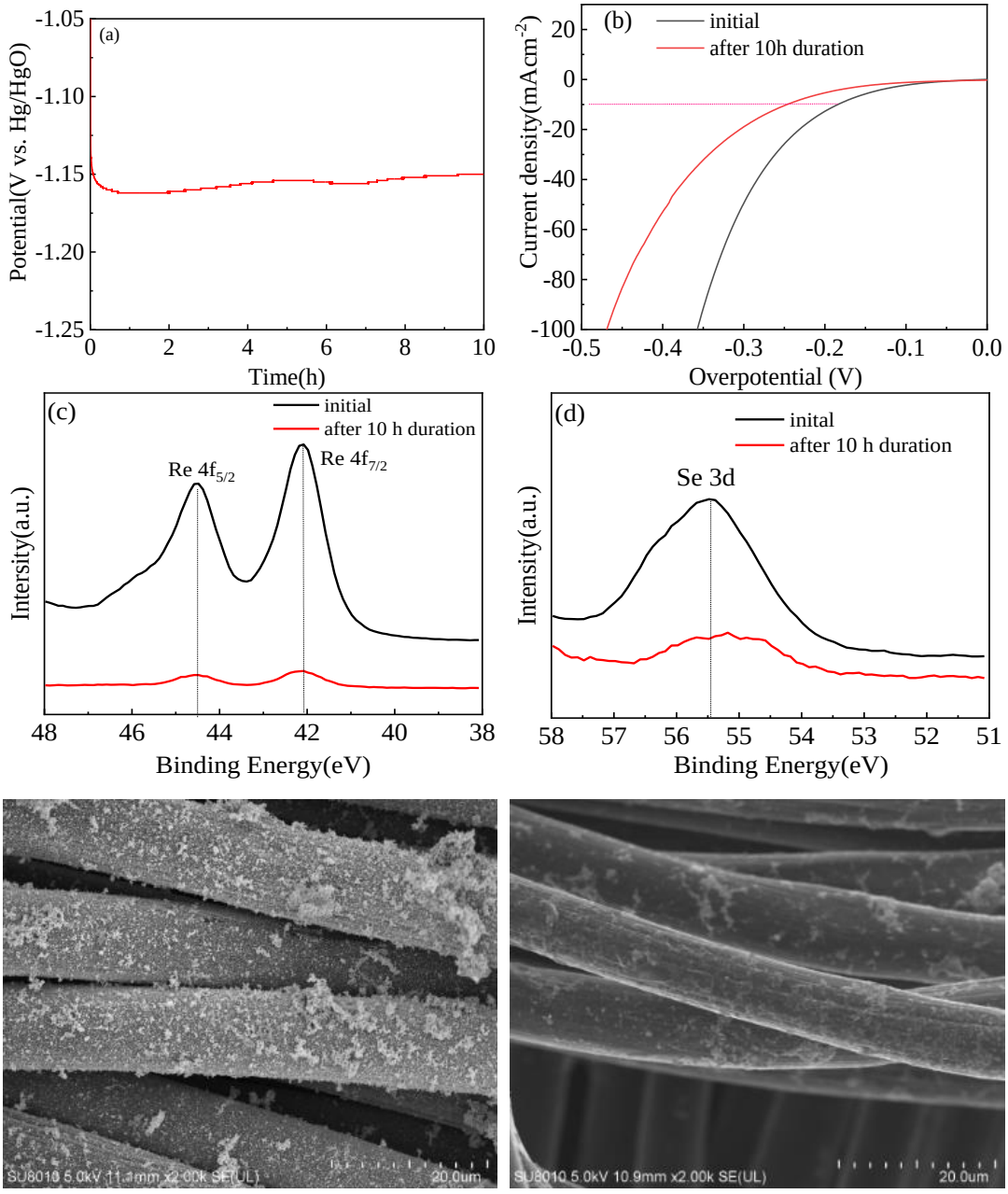

(e) *(f)*

Fig. 5. Performance Comparison for Sample C4 before and after the 10 h stability test: (a) Overpotential curve over time at current density of 10 mA cm^{-2}; (b) LSV curve; (c) Re4f high-resolution spectrum; (d)Se3d high-resolution spectrum; (e, f) SEM images.

The stability of catalyst is also a crucial factor for large-scale commercial applications. To evaluate the stability of $ReSe_2$/CC in the continuous HER process, the chronopotentiometry test

(V-t) was also performed at 10 $mAcm^{-2}$ for 10 h in 1 M KOH solution. The overpotential-time curve is shown in Fig.5a. The overpotential shows a slight increase during 10 hours of continuous HER, which demonstrae a better electrochemical stability of $ReSe_2$/CC. To further evaluate the stability of $ReSe_2$/CC, LSV, XPS and SEM were also performed before and after 10 h stability test. The results are displayed in Fig.5. After 10 h stability tests, the overpotential at 10 $mAcm^{-2}$ increased by 61mV. The positions of Re 4f and Se 3d peaks are invariable after stability tests, however, the peak intensity significantly reduced. In addition, the surface morphologies of $ReSe_2$/CC are compared at the initial stage and after stability tests, as shown in Fig. 5e and Fig. 5f, The $ReSe_2$ aggregated on CC substrate shed after stability tests. Therefore, the long-term stability of $ReSe_2$/CC catalyst needs to be further improved.

3.3. The formation mechanism and working mechanism in the HER process of ReS_2 nanosheets

The formation process of $ReSe_2$ nanosheets prepared by hydrothermal method is described as follows: In the precursor of the hydrothermal reaction NH_4ReO_4 and Se powder is used as reactant, $NaBH_4$ as a reducing agent and deionized water as solvent. Under high pressure and high temperature, Se reacts with $NaBH_4$ in aqueous solution to form Se^{2-} ions [21].

$$2Se+4BH_4^- +7H_2O \rightarrow 2Se^{2-}+B_4O_7^{2-}+2H^+ +14H_2 \quad (2)$$

ReO_4^- anion in reaction solution is reduced to Re^{4+} cation by $NaBH_4$ [21]

$$ReO_4^- + 4BH_4^- + 10H_2O \rightarrow Re^{4+}+B_4O_7^{2-}+7OH^- +29/2H_2 \quad (3)$$

Finally, the Re^{4+} and Se^{2-} reactions generate $ReSe_2$.

$$Re^{4+} + 2Se^{2-} \rightarrow ReSe_2 \quad (4)$$

The working mechanism of the HER kinetics processes of $ReSe_2$ nanosheets as HER catalysts is described as follows. [30-32]:

$$H_2O + e^- \rightarrow H^* + OH^- \quad \text{(Volmer)} \quad (5)$$

$$H^* + H_2O + e^- \rightarrow H_2 + OH^- \quad \text{(Heyrovsky)} \quad (6)$$

$$H^* + H^* \rightarrow H_2 \quad \text{(Tafel)} \quad (7)$$

where H* represents an adsorbed hydrogen atom which is generated on the $ReSe_2$ nanosheets surface by the reaction of H_2O and an electron; The working mechanism of the HER process includes two steps of hydrogen adsorption and desorption. The first step is hydrogen adsorption, where the hydrogen atoms bind to the catalyst and generate H* by the reaction of H_2O and an electron (Volmer step). The second step is hydrogen desorption, where H_2 is generated via H* reaction with H_2O and e^- (Heyrovsky step) or via two H* reaction on the $ReSe_2$ nanosheets surface (Tafel step). Therefore, Volmer-Heyrovsky and/or Volmer−Tafel mechanism is the working

mechanism for the HER process. Theoretical studies revealed that the tafel slopes of the above three reaction steps are 120, 40 and 30 $mVdec^{-1}$, respectively [19, 32]. Tafel slope is inversely proportional to reaction rate. Therefore, the Volmer step is rate-determining during the HER process, that is to say, the hydrogen absorption process of the $ReSe_2$ nanosheet catalyst determines the reaction kinetics of HER. Theoretically, the reaction rate of HER process is controlled by the Gibbs free energy (ΔG_{H^*}) of hydrogen adsorption. According to the Sabatier principle [33], the optimal catalytic activity of catalyst is obtained when ΔG_{H^*} is close to 0 eV, because the more positive ΔG_{H^*} indicate hydrogen adsorption is more difficult; while the more negative ΔG_{H^*} indicate that hydrogen desorption is more difficult. Kwak and co-workers [21] employed density functional theory (DFT) to calculate the Gibbs free energy (ΔG_{H^*}) on the basal planes of $ReSe_2$. The ΔG_{H^*} value of $ReSe_2$ with no Se vacancies is 1.74 eV; While the ΔG_{H^*} value of $ReSe_2$ with 6.25% Se vacancies is decreased to 0.15 eV. The Re-H bonds are easily formed near Se vacancies. Therefore, the coordinative-unsaturated Se edge sites and Re or Se vacancies as well as defects in basal planes can act as an effective active site for HER.

4. Conclusion

In conclusion, $ReSe_2$ were directly prepared on a carbon cloth substrate by hydrothermal synthesis technology using the reaction solution prepared using NH_4ReO_4 and Se powder as reactant, $NaBH_4$ as reducing agent and deionized water as solvent. $ReSe_2$ grown on CC substrates is composed of numerous nanosheets which gather into flower-like microspheres. The layer number of $ReSe_2$ nanosheets is approximately 3-5 layers. When the concentration of NH_4ReO_4, Se and $NaBH_4$ is 0.017 M, 0.022 M, 0.067 M and growth time of 8 h, the as-prepared $ReSe_2$ showed better HER electrocatalytic performance with an overpotential of 197 mV at a current density of 10 mA/cm^2, Tafel slope of 142 mV/dec, C_{dl} of 13 mF/cm^2 and charge transfer resistance R_{ct} of 4.13 Ω. The coordinative-unsaturated Se edge sites and Re vacancies as well as defects in basal planes can serve as an effective active site for HER. However, the stability $ReSe_2$/CC is not satisfactory due to some aggregation phenomenon of $ReSe_2$ microspheres occurring. Further works are needed to improve the uniformity and long-term stability of $ReSe_2$ nanosheets.

References

[1] J. Duan, S. Chen, B. A. Chambers, G. G. Andersson, S. Z. Qiao, Adv. Mater. 27, 4234(2015); https://doi.org/10.1002/adma.201501692

[2] N. L. Panwar, S. C. Kaushik, S. Kothari, 15, 1513-1524 (2011); https://doi.org/10.1016/j.rser.2010.11.037

[3] M. Ball, M. Wietschel, (2009) The hydrogen economy: opportunities and challenges, Cambridge University Press, England; https://doi.org/10.1017/CBO9780511635359

[4] M. Saquib, A. Halder, J. Solid State Chem. 262, 229-236 (2018); https://doi.org/10.1016/j.jssc.2018.03.030

[5] S. Su, Q. Zhou, Z. Zeng, D. Hu, X. Wang, M. Jin, X. Gao, R. Nötzel, G. Zhou, Z. Zhang, J.

Liu, ACS Appl. Mater. Interfaces 10, 8026-8035 (2018); https://doi.org/10.1021/acsami.7b19197

[6] J. Huang, Z. Wei, J. Liao, W. Ni, C. Wang, J. Ma, J. Energy Chem. 33, 100-124 (2019); https://doi.org/10.1016/j.jechem.2018.09.001

[7] S. Li, W. Zang, X. Liu, S. J. Pennycook, Z. Kou, C. Yang, C. Guan, J. Wang, Chem. Eng. J. 359, 1419-1426 (2019); https://doi.org/10.1016/j.cej.2018.11.036

[8] M. P. Aparna, R. Chatanathodi, ACS Appl. Nano Mater. 5, 2385-2394 (2022); https://doi.org/10.1021/acsanm.1c04070

[9] S. Ng, C. Iffelsberger, Z. Sofer, M. Pumera, Adv. Funct. Mater. 30, 1910193 (2020); https://doi.org/10.1002/adfm.201910193

[10] Y. Yan, S. Xu, H. Li, N. C. S. Selvam, J. Y. Lee, H. Lee, P. J. Yoo, Chem. Eng. J. 405, 126728 (2021); https://doi.org/10.1016/j.cej.2020.126728

[11] L. Wang, Z. Sofer, J. Luxa, D. Sedmidubský, A. Ambrosi, M. Pumera, Electron. Commun. 63, 39-43 (2016); https://doi.org/10.1016/j.elecom.2015.11.011

[12] Y. Zhou, E. Song, J. Zhou, J. Lin, R. Ma, Y. Wang, W. Qiu, R. Shen, K. Suenaga, Q. Liu, J. Wang, Z. Liu, J. Liu, ACS Nano 12, 4486-4493 (2018); https://doi.org/10.1021/acsnano.8b00693

[13] Y. C. Lin, H.P. Komsa, C. H. Yeh, T. Björkman, Z.Y. Liang, C. H. Ho, Y. S. Huang, P. W. Chiu, A. V. Krasheninnikov, K. Suenaga, ACS Nano 9, 11249-11257 (2015); https://doi.org/10.1021/acsnano.5b04851

[14] Q. Sun, B. Zhang, L. Diao, B. Chen, K. Song, L. Ma, F. He, J. Mater. Chem. A 8, 11607−11616 (2020); https://doi.org/10.1039/D0TA02683B

[15] J. Li, Y. Liu, C. Liu, W. Huang, Y. Zhang, M. Wang, Z. Hou, X. Wang, M. Jin, G. Zhou, X. Gao, Z. Zhang, J. Liu, Chem. Commun. 56, 305−308 (2020); https://doi.org/10.1039/C9CC08076G

[16] M. Zhuang, G. L. Xu, L. Y. San, Y. Dou, C. J. Sun, X. Ou, Y. Xie, Z. Liu, Y. Cai, Y. Ding, I.H. Abidi, A. Tyagi, K. Amine, Z. Luo, Nano Energy 58, 660−668 (2019); https://doi.org/10.1016/j.nanoen.2019.01.093

[17] J. Huang, H. Gao, Y. Xia, Y. Sun, J. Xiong, Y. Li, S. Cong, J. Guo, S. Du, G. Zou, Nano Energy 46, 305−313 (2018); https://doi.org/10.1016/j.nanoen.2018.02.003

[18] X. Xu, H. Zhao, R. Wang, Z. Zhang, X. Dong, J. Pan, J. Hu, H. Zeng, Nano Energy 48, 337−344 (2018); https://doi.org/10.1016/j.nanoen.2018.03.078

[19] J. Luxa, P. Marvan, P. Lazar, Z. Sofer, Nanoscale 11, 14684-14690 (2019); https://doi.org/10.1039/C9NR03281A

[20] J. Pan, R. Wang, X. Xu, J. Hu, L. Ma, Nanoscale 11, 10402−10409 (2019); https://doi.org/10.1039/C9NR00997C

[21] I. H. Kwak, I. S. Kwon, T. T. Debela, H. G. Abbas, Y. C. Park, J. Seo, J. P. Ahn, J. H. Lee, J. Park, H. S. Kang, ACS Nano 14, 11995-12005 (2020); https://doi.org/10.1021/acsnano.0c05159

[22] Y. Yan, S. Xu, H. Li, N. C. S. Selvam, J. Y. Lee, H Lee, P. J. Yoo, Chem. Eng. J. 405, 126728 (2021); https://doi.org/10.1016/j.cej.2020.126728

[23] R. Wang, J.C. Han, P. Xu, T. L. Gao, J. Zhong, X. J. Wang, X. H. Zhang, Z. J. Li, L. L. Xu, B. Song, Adv. Sci. 7, 2000216 (2020); https://doi.org/10.1002/advs.202000216

[24] C. Wang, S. Yang, W. Xiong, C. Xia, H. Cai, B. Chen, X. Wang, X. Zhang, Z. Wei, S. Tongay, J. Li, Q. Liu, Phys. Chem. Chem. Phys. 18, 27750-27753 (2016);

https://doi.org/10.1039/C6CP04752A

[25] S. Jiang, Z. Zhang, N. Zhang, Y. Huan, Y. Gong, M. Sun, J. Shi, C. Xie, P. Yang, Q. Fang, H. Li, L .Tong, D. Xie, L. Gu, P. Liu, Y. Zhang, Nano Res. 11, 1787-1797 (2018); https://doi.org/10.1007/s12274-017-1796-8

[26] L. F. Deng, X. Y. Zhang, J. Liu, A. X. Wei, Y. D. He, Z. Liu, N.Q. Luo, 24, 14479-14487 (2022); https://doi.org/10.1039/D2CP01215D

[27] Y. Liu, J. Li, W. Huang, Y. Zhang, M. Wang, X. Gao, X. Wang, M. Jin, Z. Hou, G. Zhou, Z. Zhang, J. Liu, ACS Appl. Mater. Interfaces 12, 33586-33594 (2020) https://doi.org/10.1021/acsami.0c02951

[28] Y. Y. Chen, Y. Zhang, W. J. Jiang, X. Zhang, Z. Dai, L. J. Wan, J. S. Hu, ACS Nano 10, 8851-8860 (2016); https://doi.org/10.1021/acsnano.6b04725

[29] J. Li, Q. Zhou, C. Yuan, P. Cheng, X. Hu, W. Huang, X. Gao, X. Wang, M. Jin, R. Notzel, G. Zhou, Z. Zhang, J. Liu, J. Colloid Interface Sci. 553, 699-704 (2019); https://doi.org/10.1016/j.jcis.2019.06.073

[30] Q. Zhu, Y. Qu, D. Liu, K.W. Ng, H. Pan, ACS Appl. Nano Mater. 3, 6270-6296 (2020); https://doi.org/10.1021/acsanm.0c01331

[31] J. X. Zhang, A. X. Wei, J. Liu, J. L. Zhu, Y. D. He, Z. Liu, J. Alloys Compd. 927, 166990(2022); https://doi.org/10.1016/j.jallcom.2022.166990

[32] R. Chen, Y. Ao, C. Wang, P. Wang, Chem. Commun. 56, 8472-8475 (2020); https://doi.org/10.1039/D0CC01300E

[33] J. Ran, H. Zhang, J. Qu, J. Shan, S. Chen, F. Yang, R. Zheng, J. Cairney, L. Song, L. Jing, S. Z. Qiao, ACS Mater. Lett. 2, 1484-1494 (2020); https://doi.org/10.1021/acsmaterialslett.0c00205